Long-term potentiation expands information content of hippocampal dentate gyrus synapses

Cailey Bromer[a,b], Thomas M. Bartol[a], Jared B. Bowden[c,d,e], Dusten D. Hubbard[c,d], Dakota C. Hanka[c,d], Paola V. Gonzalez[c,d], Masaaki Kuwajima[c,d], John M. Mendenhall[c,d], Patrick H. Parker[c,d], Wickliffe C. Abraham[e,1], Terrence J. Sejnowski[a,b,1], and Kristen M. Harris[c,d,1]

[a]Computational Neurobiology Laboratory, The Salk Institute for Biological Sciences, La Jolla, CA 92037; [b]Division of Biological Sciences, University of California, San Diego, La Jolla, CA 92093; [c]Center for Learning and Memory, The University of Texas at Austin, Austin, TX 78712-0805; [d]Department of Neuroscience, The University of Texas at Austin, Austin, TX 78712-0805; and [e]Department of Psychology, University of Otago, 9016 Dunedin, New Zealand

Contributed by Terrence J. Sejnowski, January 16, 2018 (sent for review September 18, 2017; reviewed by Gary Lynch and Hyunjune Sebastian Seung)

An approach combining signal detection theory and precise 3D reconstructions from serial section electron microscopy (3DEM) was used to investigate synaptic plasticity and information storage capacity at medial perforant path synapses in adult hippocampal dentate gyrus in vivo. Induction of long-term potentiation (LTP) markedly increased the frequencies of both small and large spines measured 30 minutes later. This bidirectional expansion resulted in heterosynaptic counterbalancing of total synaptic area per unit length of granule cell dendrite. Control hemispheres exhibited 6.5 distinct spine sizes for 2.7 bits of storage capacity while LTP resulted in 12.9 distinct spine sizes (3.7 bits). In contrast, control hippocampal CA1 synapses exhibited 4.7 bits with much greater synaptic precision than either control or potentiated dentate gyrus synapses. Thus, synaptic plasticity altered total capacity, yet hippocampal subregions differed dramatically in their synaptic information storage capacity, reflecting their diverse functions and activation histories.

dentate gyrus | plasticity | synapse | information theory | granule cell

Evidence for Hebbian plasticity—such as long-term potentiation (LTP), long-term depression (LTD), and spike timing-dependent plasticity—is abundant in the hippocampus, neocortex, and many other brain regions (1–3). The literature highlights the importance of the timing of axonal input relative to postsynaptic cell depolarization for achieving changes in synaptic efficacy. Notably, changes in synapse size that are relevant to these forms of plasticity have been observed frequently and are well correlated across several metrics, including spine head volume, postsynaptic density (PSD) area, and presynaptic vesicle number (4–13). Importantly, pairs of spines sharing a dendrite and an axonal input tend to be similar in size across the broad range in spine sizes (14–17). The tendency for spines with this presumed shared activation history to have similar size is likely not an accident, but rather a reflection of the shared Hebbian processes at work. These natural tendencies prompted the use of signal detection theory to estimate the number of distinguishable states that a dendritic spine synapse can assume. The outcome of these calculations for hippocampal area CA1 yielded 26 distinct states (4.7 bits) for spines on pyramidal cell dendrites (18).

Here, we applied signal detection theory to establish the information storage capacity of synapses on granule cell dendrites in the middle molecular layer (MML) of the dentate gyrus. We assessed whether this capacity is altered in response to LTP in vivo and differs from area CA1 synapses. The hippocampal dentate gyrus is an intriguing structure, being one of the few mammalian brain regions capable of neurogenesis in adulthood and exhibiting synaptic plasticity that is influenced by relative neuronal age (19, 20). Learning-related stimulation paradigms implemented in the dentate gyrus have also revealed a low threshold for intrinsic plasticity (21). The dendritic arbors offer additional important distinguishing features; in contrast to the CA1 pyramidal cells, the dentate granule cells lack an apical trunk and basilar dendrites. Instead, the dentate granule cells exhibit a chalice-shaped arbor that is associated with poor backpropagation of action potentials (22). For these reasons, the degree of correlation in the strengths of the synapse pairs sharing a presynaptic and postsynaptic history may be less for granule cells than for pyramidal cells.

Analyses from three-dimensional electron microscopy (3DEM) revealed a marked expansion in the dynamic range of synapse sizes and decrease in coefficient of variation (CV) after LTP induction in the dentate gyrus. These changes resulted in a substantial increase in information storage capacity that was, nonetheless, well below the capacity of even control CA1 synapses.

Results

LTP Expands the Distribution of Spine Sizes Relative to Control Stimulation. To induce LTP in the dentate MML of freely moving rats, we used the previously described methods of Bowden et al. (23). Briefly, stimulating electrodes were surgically implanted in both the medial and lateral perforant paths of the LTP

Significance

Understanding plasticity processes in the hippocampus is critical to our understanding of the biological underpinnings of memory. By applying information theory to quantify information content at synapses, we demonstrate that induction of long-term potentiation (LTP) increases the storage capacity of synapses in hippocampal dentate gyrus. Nevertheless, even after LTP, the information storage capacity of dentate synapses was much lower than in a different part of the hippocampus, area CA1. This work lays a foundation for future studies elucidating the time course for increased information storage content as well as the basis for interregion variability in information storage capacity.

Author contributions: C.B., T.M.B., J.B.B., D.D.H., D.C.H., P.V.G., M.K., J.M.M., P.H.P., W.C.A., T.J.S., and K.M.H. designed research; C.B., T.M.B., T.J.S., and K.M.H. designed and applied the information theory to the analyses; C.B., T.M.B., J.B.B., D.D.H., D.C.H., P.V.G., M.K., J.M.M., and P.H.P. performed research; J.B.B., M.K., J.M.M., W.C.A., and K.M.H. designed and performed the electrophysiology experiments, tissue processing, and imaging; C.B., J.B.B., D.D.H., D.C.H., P.V.G., M.K., P.H.P., and K.M.H. performed and curated reconstructions; C.B., T.M.B., D.D.H., W.C.A., T.J.S., and K.M.H. analyzed data; C.B., T.M.B., J.B.B., D.D.H., D.C.H., P.V.G., M.K., J.M.M., P.H.P., W.C.A., T.J.S., and K.M.H. wrote the paper.

Reviewers: G.L., University of California, Irvine; and H.S.S., Princeton University.

Conflict of interest statement: T.J.S. and Gary Lynch were coauthors on a 2014 review article.

Data deposition: The output text files from Blender Reconstructions of EM Data and accompanying Python analysis scripts reported in this paper have been deposited at www.mcell.cnl.salk.edu/models/dentate-gyrus-spine-analysis-2018-1.

[1]To whom correspondence may be addressed. Email: cabraham@psy.otago.ac.nz, terry@salk.edu, or kmh2249@gmail.com.

This article contains supporting information online at www.pnas.org/lookup/suppl/doi:10.1073/pnas.1716189115/-/DCSupplemental.

hemisphere, and a further stimulating electrode was implanted in the medial path of the control hemisphere. Field potential recordings were made alternately between hemispheres using electrodes placed bilaterally in the dentate hilus. LTP was induced in two animals by 50 trains of unilateral delta-burst stimulation (DBS) to the medial path electrode, and then recorded for 30 min, timed from the beginning of the DBS. Relative to control hemispheres (Fig. 1*A*), the LTP hemispheres (Fig. 1*B*) showed an average of 41.0% (33.6% and 48.3%) potentiation in the MML.

Serial electron micrographs were imaged from the control MML (Fig. 1*C*) and LTP MML (Fig. 1*D*). Three-dimensional reconstructions were made of dendritic spines and synapses occurring along the full length of three dendrites from each of the control hemispheres (Fig. 1*E*) and each of the LTP hemispheres (Fig. 1*F*). Axons that were presynaptic to at least 1 of 15 of the dendritic spines along an intermediate component of the dendritic segment were traced to determine whether they made more than one synapse along the same dendrite and are referred to as same dendrite/same axon (SDSA) pairs (Fig. 1 *E* and *F*). All 3DEM reconstructions and measurements were obtained blind as to the hemisphere being analyzed.

We hypothesized that individual dendritic spines would be in flux during this early phase in the expression of LTP. To test this hypothesis, each reconstructed dendritic spine was transferred to the Neuropil Tools analyzer in Cell Blender (*Methods*) to obtain

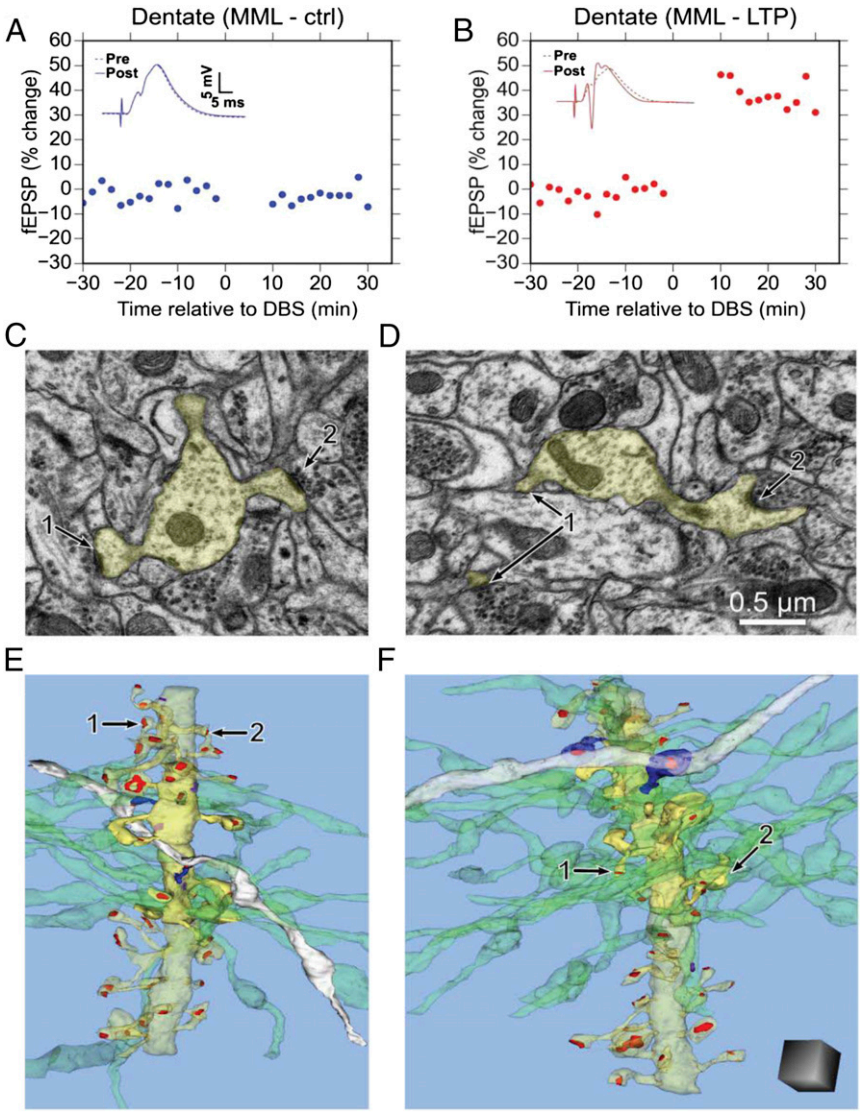

Fig. 1. Induction of LTP and representative dendritic spines from the control and LTP hemispheres. (*A*) Control hemispheres received test pulses only to the contralateral medial perforant pathway throughout the experiment. (*B*) LTP was induced by DBS in the ipsilateral hemispheres (at time 0). Graphs in *A* and *B* illustrate the average change relative to baseline stimulation in fEPSP response relative to baseline stimulation (0% for controls and 33.6% and 48.3%, respectively, for the LTP hemispheres). *Insets* show representative waveforms from baseline responses (dotted pre) superimposed by responses for each hemisphere (smooth post) following DBS in the LTP hemisphere. Example electron micrographs from a series in the (*C*) control and (*D*) LTP hemispheres. (Scale bar in *D* is for *C* and *D*.) Arrows indicate representative dendritic spines from each condition and match the arrows pointing to the same spines in the 3DEM scenes below from the (*E*) control hemisphere (total dendrite length, 8.98 μm) and (*F*) LTP hemisphere (total dendrite length, 9.60 μm). The length of the reconstructed dendrites analyzed for presynaptic connectivity (solid yellow) revealed that most of the axons (green) made synapses with just one dendritic spine. In each of these examples, one axon (white) made synapses with two of the dendritic spines (blue); these are referred to as same dendrite/same axon (SDSA) pairs. The dendritic shaft and spines occurring along the rest of the reconstructed dendrite are illustrated in translucent yellow. All excitatory synapses are illustrated in red, and the inhibitory synapses in purple. [Scale cube (in *F*): 1 μm^3 for *E* and *F*.]

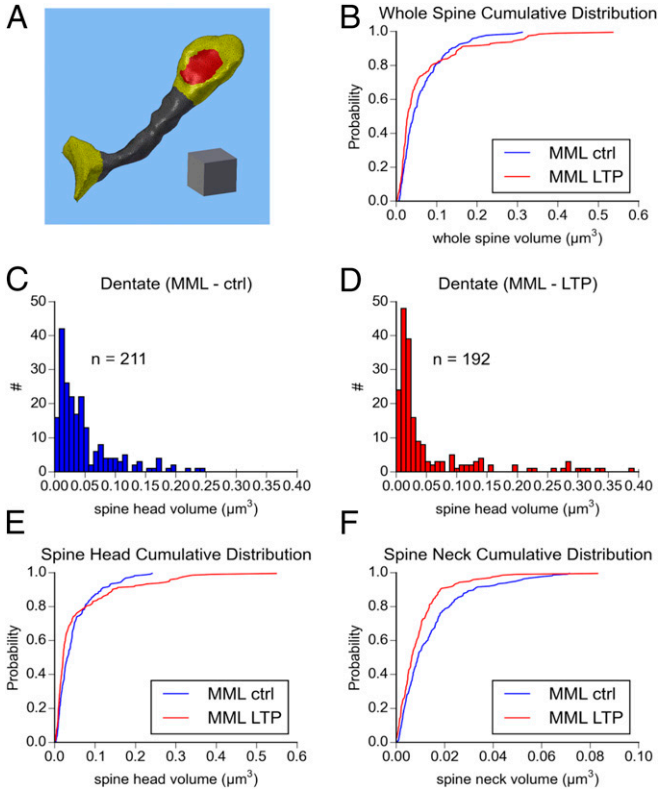

Fig. 2. By 30 min after induction, LTP shifts the distribution of spine volumes relative to the control condition. (*A*) The spine volume measurements were obtained using Neuropil Tools to edit each spine into its components, represented with the connection to the dendritic shaft in yellow, the neck in dark gray, and the PSD area in red located on the yellow head. The tube is 0.25 μm on a side. (*B*) Cumulative distribution plot showing that the two spine populations were significantly different as measured by whole-spine volume [Kolmogorov–Smirnov (KS) test value of $P = 0.002$]. Spine head volumes for spines in the dentate gyrus MML from (*C*) control and (*D*) LTP hemispheres. (*E*) Cumulative distribution plot showing the two spine populations were significantly different as measured by head volume (KS test value of $P = 0.001$), with more of the spines in the LTP hemispheres having smaller and larger head volumes than the controls. (*F*) Cumulative distribution plot showing that the LTP spine neck volumes were significantly lower than in the controls (KS test value of $P = 0.001$).

accurate volume measurements and precise divisions of each spine into head and neck compartments, and from the dendrite shaft (Fig. 2*A*). Using 3D visualization, spine heads were digitally separated from the neck halfway along the concave arc where the head narrowed, and spine necks were similarly separated from the dendritic shaft. The distribution of whole spine volumes shifted rapidly and dramatically after the induction of LTP, such that within 30 min there were substantially more of both small and large dendritic spines (Fig. 2*B* and Fig. S1).

The edited head volumes followed the same shift in distribution as total spine volume, such that control spines had no head volumes greater than 0.25 μm^3 (Fig. 2*C*), while LTP resulted in a marked increase both in small spine head volumes less than 0.05 μm^3 and those greater than 0.25 μm^3 (Fig. 2*D*). In the cases of both spine head and whole-spine distributions, it is possible that the shift in the distribution is not uniform; in other words, it may be that enlargement of some spines results in a reduction in the size of many smaller spines. Previous work from the literature provides evidence that spine volume is redistributed in a homeostatic way following LTP (10, 24). Furthermore, concurrent LTD is known to accompany LTP in the dentate gyrus, and the sampling zone may have contained both potentiated and depressed synapses, which would account for this expansion (25, 26). Determination of which spines will grow may be influenced by prior activity or learning (27–30).

The cumulative distributions of spine head volumes were significantly different between control and LTP hemispheres, with an increase in both tails of the distribution (Fig. 2*E*). This effect could be discerned in the dendrites from both animals (Fig. S2). In contrast, the neck volumes were uniformly smaller following LTP induction relative to control (Fig. 2*F* and Fig. S3). This observation suggests that spine volume could be redistributing between the neck and head. Such redistribution would make the junction between the head and neck less obvious. Indeed, when four head–neck determinations were made on each spine by two people, the four measurements were highly similar for the 211 control spine heads, whereas marked discrepancies were apparent among the 192 LTP spines (Fig. S4).

To evaluate whether the increase in both small and large spine heads resulted in a balanced total synaptic input, we performed an unbiased dendritic segment analysis based on the reconstructions of the intermediate portions of the dendritic segments (solid yellow, Fig. 1 *E* and *F*). None of the findings could be explained by changes in the number of spines, axons, or SDSAs per micrometer length of dendrite, which were similar between the control and LTP dendrites (Fig. 3*A* and Table 1). Furthermore, the summed asymmetric synaptic area across all synapses per micrometer of dendritic length was constant across the control and LTP conditions (Fig. 3*B*). Thus, the enlargement of some spines was counterbalanced by shrinking of others, and the summed synaptic input remained constant along these local stretches of dendrite.

Together, these findings suggest that, following the induction of LTP, there was a rapid and robust redistribution of spine volume from the neck into the head that occurred at enlarging spines, while another population of spines shrank to counterbalance this growth.

LTP Increases Information Storage Capacity at Synapses in Dentate MML. Signal detection theory was used to determine whether the expanded spine distribution following induction of LTP elevated information storage capacity at the MML synapses. Spine head volume is well correlated with other measures of synaptic efficacy; hence the principles of signal detection theory were applied to the range of observed spine head sizes to calculate the number of distinguishable synaptic states and bits of precision in each condition. The number of distinguishable spine sizes (which corresponds

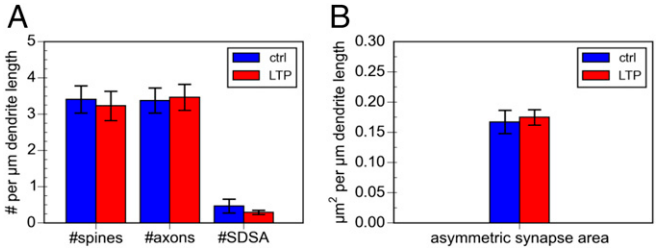

Fig. 3. No change in the number of spines, axons, or SDSAs, or in the summed synaptic area per unbiased length of dendrite. (*A*) Bar plot illustrating the number (per micrometer length of dendrite, mean ± SEM) of spines, axons, and axons participating in SDSA pairs shows no significant difference between control (ctrl) and LTP hemispheres (ANOVAs: spines [$F_{(1,10)} = 0.11$, $P = 0.75$]; axons [$F_{(1,10)} = 0.03$, $P = 0.87$]; SDSA [$F_{(1,10)} = 0.75$, $P = 0.41$]). Here, the SDSA pairs included all types shown in Table 1 (spine–spine, multisynaptic spine–spine, quadruplet, and spine–shaft). (*B*) The total asymmetric synapse area (based on the summed PSD area per micrometer, including spines and asymmetric shaft synapses) was also similar between the two conditions [$F_{(1,10)} = 0.11$, $P = 0.75$].

Table 1. Sources of data samples

Condition	Control	Control	LTP	LTP
Animal	Rat 1	Rat 2	Rat 1	Rat 2
No. dendrites	3	3	3	3
Total length, μm	30.04	27.56	28.65	29.35
No. spines	122	73	104	74
No. heads	129	82	112	78
Intermediate dendritic segments				
Length, μm	11.91	17.65	12.89	19.17
No. spines	50	46	51	47
No. axons	48	47	53	53
No. SDSAs total	8	5	4	5
No. SDSAs included for CV	6	4	4	4
No. synapses	58	53	53	56
No. spine synapses	52	49	48	50
No. asymmetric shaft synapses	1	1	1	3
No. symmetric shaft synapses	5	3	4	3

The top portion of this table represents the fully reconstructed dendritic segments including all of the spine synapses for Figs. 1, 2, 5, and 6. The intermediate dendritic segments were used for Figs. 3 and 4. Branched spines were considered as one spine, but each head was analyzed separately for volume. The total SDSAs included pairs of spines, each with a single synapse; one case of a spine paired with a shaft synapse; and two cases of spines paired with multisynaptic spines. Only the SDSAs between two spines with one synapse each were included in the CV analysis (10 control, 8 LTP).

to bits) is calculated as the number of distinct Gaussian distributions that together span the entire range of observed spine head sizes. The observed range is used to set a "hypothetical" range of possible sizes for the signal detection theory equation. Importantly, the number of spines in each size bin in the observed range does not affect the "hypothetical" range. The number of distinguishable spine sizes is directly proportional to this range in size and inversely proportional to the CV between pairs of spine head volumes (18, 31). The resulting bits of information storage is a logarithm base 2 of this ratio (see *Methods* for equations). Hence, the observed increase in size range following LTP would retain the same amount of information storage capacity only if the CV among the coactivated synapses increased proportionately.

The minimum CV occurs between two spines with shared activation history, and these are used to determine the lower limit of information storage capacity (18). Pairs of spines that arise from the same dendritic branch and form synapses with the same axonal input (SDSAs, e.g., Fig. 1 *E* and *F*) are assumed to have the most similar activation histories. The more identical two spines are to one another in volume, the closer the slope of regression line will be to 1 (Fig. 4). Interestingly, the slopes of the regression lines regarding the spine head volumes for the SDSA pairs were not statistically different across control (Fig. 4*A*) and LTP (Fig. 4*B*) hemispheres, or from random pairings of spine head volumes. The median CV did not differ significantly between conditions; however, the absolute value for the median CV was markedly lower for the LTP (0.26 ± 0.09) than the control (0.46 ± 0.08) SDSA pairs. The CVs were similar across the range in SDSA spine head volumes for the control (Fig. S5*A*) or the LTP conditions (Fig. S5*B*). Hence, small spines were just as precise as large spines in both conditions and the similarity between spines with shared activation histories was independent of spine size.

Given the CV in head size between the coactivated (SDSA) synapses, the spacing between the mean values of each subdistribution can be chosen to achieve a total of 31% overlap with adjacent subdistributions having a 69% discrimination threshold, which corresponds to a signal-to-noise ratio of 1. This threshold estimates the minimum spacing between distinguishable spine head volumes; namely, how many meaningful "buckets" spines fall into. Using the median control CV (0.46) and range (73.3, Fig. 2*C*), we calculated 6.5 distinguishable spine head volumes (Fig. 4*C*) and thus 2.7 bits of information storage capacity per synapse. In contrast, the same signal detection theory calculations for the LTP median CV (0.26) and range (236.2, Fig. 2*D*) revealed the information storage capacity increased to 12.9 distinguishable spine sizes (Fig. 4*D*), giving 3.7 bits per synapse following the induction of LTP. Thus, the increase in information storage capacity, resulting from the increase in the number of distinguishable spine sizes represented in Fig. 4 *C* and *D*, was enabled by the reduced CV among coactivated synapses and expanded range in spine sizes following LTP.

Dimensions and Information Storage Capacity Differ Between Dentate Gyrus and CA1 Synapses. To determine whether differences in spine dimensions affected information storage capacity across brain regions, we compared synapses from both conditions in the dentate gyrus MML (Fig. 5 *A*–*C*) with those in stratum radiatum of hippocampal area CA1 (Fig. 5 *D*–*F*). The overall distribution of spine head volumes from dentate MML (Fig. S6*A*) relative to those in stratum radiatum of CA1 (Fig. S6*B*) had a cumulative distribution that was significantly right-shifted (larger) for dentate [Kolmogorov–Smirnov (KS) value of $P <$ 5e-5; Fig. S6*C*].

Combining across the control and LTP hemispheres, the slope of the SDSA paired spine volumes was lower in the MML (0.64, Fig. 6*A*) than in CA1 (0.91, Fig. 6*B*). A greater variability was also evidenced by the higher CV for SDSA pairs in dentate

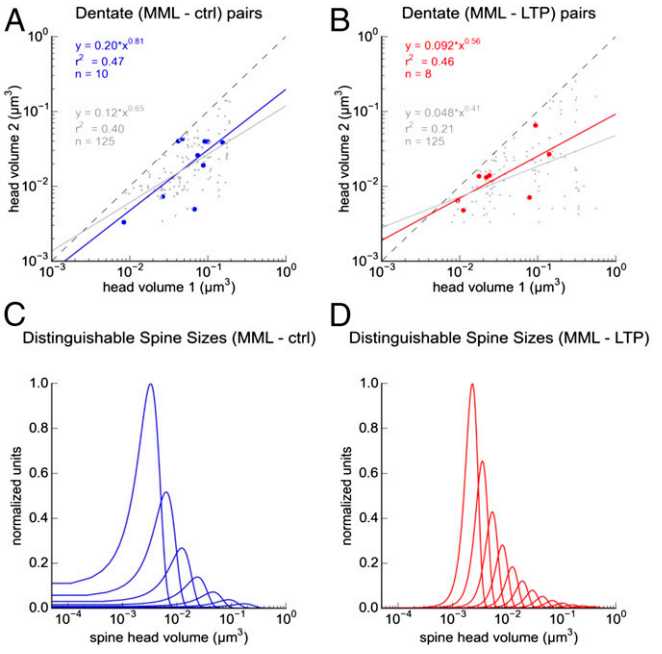

Fig. 4. LTP increased information storage capacity at synapses in dentate gyrus MML by decreasing CV and expanding the range. (*A*) SDSA spine head volumes under control condition (blue data; slope of 0.81, median CV of 0.46) compared with random pairings between unshared control spines (gray data; line slope of 0.65, median CV of 0.46). (*B*) SDSA spine head volumes under LTP condition (red data; slope of 0.56, median CV of 0.26) compared with random pairs of unshared LTP spines (gray data; slope of 0.41, median CV of 0.47). ANCOVA on the slopes for the control vs. LTP, value of $P = 0.54$; for control vs. random pairs, value of $P = 0.53$; or for LTP vs. random pairs, value of $P = 0.65$. In addition, the median CVs for the SDSA pairs did not differ between the control (0.46 ± 0.08) and LTP (0.26 ± 0.09) conditions (Kruskal–Wallis H test = 0.64, $P = 0.42$). (*C*) Distinguishable spine sizes under control condition (6.5). (*D*) Distinguishable spine sizes under LTP condition (12.9).

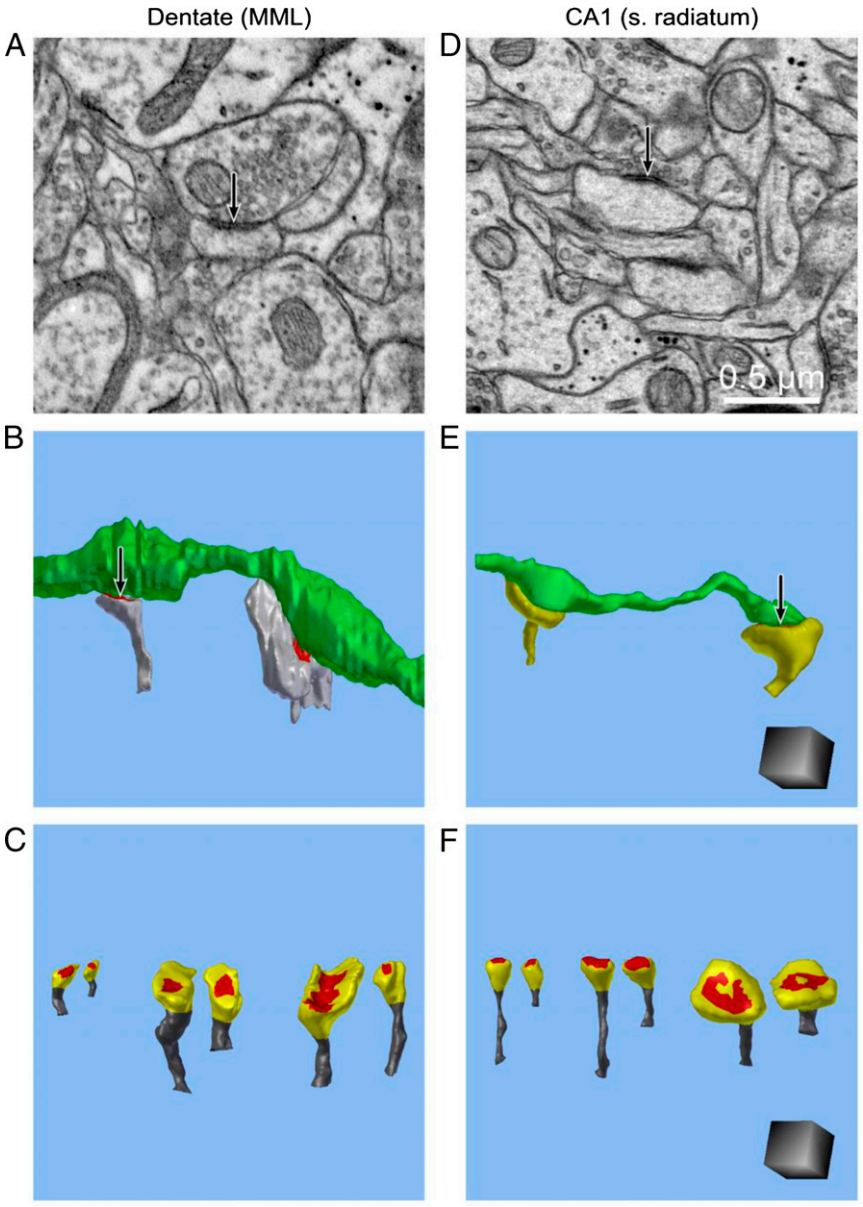

Fig. 5. SDSA pairs in dentate MML compared with SDSA pairs in stratum radiatum of hippocampal area CA1. Examples of (*A*) EM, (*B*) 3DEM, and (*C*) SDSA pairs from smallest, median, and largest spine pairs in the control dentate MML sample. Examples of (*D*) EM, (*E*) 3DEM, and (*F*) SDSA pairs from smallest, median, and largest pairs from CA1 synapses [from Bartol et al. (18) sample]. [Scale cube in *E* and *F* are 0.5 μm on each side (0.125 μm^3) and are also for *B* and *C*, respectively.]

MML (CV = 0.40 ± 0.08) than CA1 stratum radiatum (CV = 0.10 ± 0.04). These analyses indicate that there was less concordance in spine head size for dentate SDSA pairs than for CA1 SDSA pairs. As indicated above, we calculated ∼2.7 bits of information storage capacity across the range in head volume of 73.3 in control dentate MML and ∼3.7 bits across the range of 236.2 after LTP induction in dentate MML. These outcomes indicate that, despite the increased range in spine sizes and smaller CV in SDSA pairs found after LTP induction, there was a substantially lower information storage capacity for synapses in the dentate MML (Fig. 6*C*) than in stratum radiatum of area CA1 (Fig. 6*D*, 4.7 bits) (18). This effect was due to the lower CV among coactivated synapses in CA1 stratum radiatum that was not compensated for by the broader range in spine head volumes in dentate MML.

Discussion

The log-normal distributions of synapse size and other neuronal metrics have been well documented (32). Application of a new signal detection modeling paradigm illustrates how information content can be affected by altering the CV among coactivated synapses and/or broadening the range of synapse dimensions (18). The dendritic spines of dentate granule cells are the sites where the predominant stream of information from cortex arrives in the hippocampus. The findings presented here provide evidence that synaptic plasticity can rapidly influence the information storage capacity of synapses in dentate gyrus MML. At 30 min following the induction of LTP in vivo, the range in spine size expanded, interestingly, with an increase in the frequency of both small and large spines, which was also accompanied by an improvement in precision (i.e., decrease in CV). In

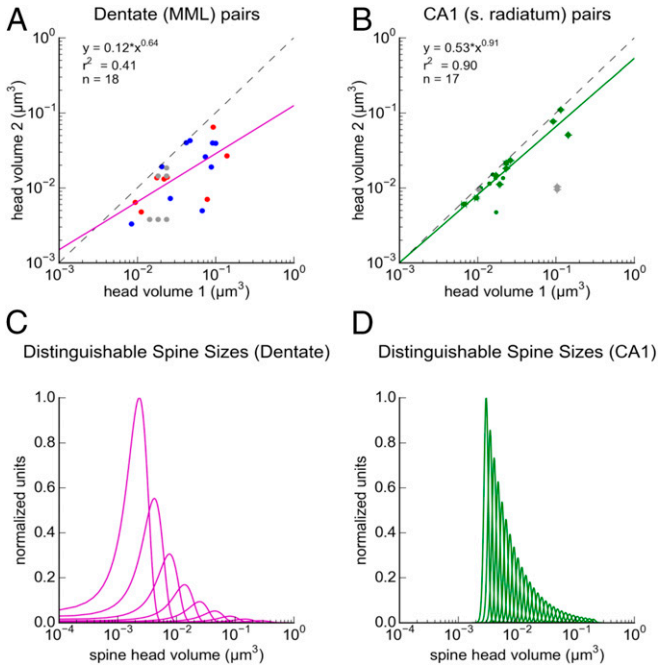

Fig. 6. Spines in CA1 stratum radiatum have more distinguishable sizes because the CV for spine head volumes among SDSA pairs was smaller than in dentate gyrus MML. (*A*) Spine head volumes from dentate gyrus MML with slope of 0.64 and CV of 0.40. (Control points in blue, LTP points represented in red. Gray points represent a quadruplet of spines sharing a dendritic branch and a single axonal input, which were excluded from the regression analyses here and above in Fig. 4*A*.) (*B*) Spine head volumes in CA1 stratum radiatum with slope of 0.91 and CV of 0.10. (Gray points represent a triplet of spines sharing a dendritic branch and single axonal input, which was excluded from the regression analyses.) (*C*) Distinguishable spine head sizes in dentate gyrus MML was 9.2 across the 236-fold range, including LTP. (*D*) Distinguishable spine head sizes in CA1 stratum radiatum was 27.5 across the 72-fold range measured in Bartol et al. (18).

contrast, spine neck dimensions were consistently diminished relative to control.

This expansion in the spine size distribution may be temporary, because the spines appeared to be in flux as manifested by the less uniform head–neck junctions in the LTP vs. the control hemispheres. Furthermore, the expansion in the spine size distribution appears to involve a homeostatic mechanism where some given population of spines shrinks as a population of fewer spines expands in size. If the observed increase in range and CV are temporary, the effect would be to privilege salient inputs and stifle less important inputs locally on the dendritic branch or globally over the whole neuron. Depending on whether the effect is local or global, the "privileged" synapses could preferentially influence dendritic computation or cell firing, respectively. Augmentation of certain spines by a "priming" activation could play a role in selecting the population of spines that undergo LTP (27–30). Additional studies of information storage at later time points following LTP stimulation will help to inform the nature and duration of the increase in information storage capacity observed at 30 min.

The total number of spines and summed synaptic area per unit length of dendrite remained constant across conditions, suggesting that enlargement of some and shrinkage of other preexisting spines occurred with LTP onset. This constancy in total synaptic input is likely due to concurrent heterosynaptic LTD in the MML, which is known to happen in neighboring nonpotentiated synapses (26). Thus, the lower CV measured for spine pairs with shared activation histories (together with the expanded range in spine size) accounts for the greater information storage capacity following LTP. Nevertheless, even the LTP-expanded range and reduced CV in the dentate gyrus MML did not bring the calculated information storage capacity close to that of CA1 stratum radiatum. The difference between regions lies primarily in the CV of SDSA paired spines with similar activation histories (CA1, 0.10; dentate overall, 0.40) because the full observed range of spine sizes in CA1 was substantially less than dentate gyrus MML (CA1, 72; dentate overall, 236). Although these measurements are based on a relatively small sample of synaptic spines, the reported differences are highly significant because of the large effect sizes.

Computers store information through their transistors, each of which has one binary bit with two possible states (0 or 1), only one of which can be assumed at any moment. Clearly, synapses in both hippocampal subregions are not simple two-state machines. Following LTP, MML in hippocampal dentate gyrus obtained about 3.7 bits per synapse with 12.9 distinguishable states compared with 4.7 bits per synapse with 26 distinguishable states in control CA1 stratum radiatum. Thus, the mechanisms responsible for these rapid morphological changes must have the same or greater precision than those leading to longer-term changes. This places constraints on amount of averaging that must take place to overcome variability from the stochastic release of neurotransmitter at these synapses (18).

At 2 h after the induction of LTP in area CA1, growth of synapse size is perfectly counterbalanced by fewer spines per unit length of dendrite (10). Although this LTP-mediated shift in CA1 has not been subjected to the signal detection analyses, the findings suggest that LTP might further separate CA1 from dentate. The difference between regions could be accounted for functionally by a number of factors. The first factor is the variable age of dentate granule cells that results from neurogenesis, including the hypothesized retirement of older neurons from participation in Hebbian learning processes (20, 33). Although we do not know the age of the granule cells that form the prepost coupled synapses, such neurogenesis does not occur in adult area CA1; thus, differential opportunities for shared presynaptic–postsynaptic interactions might contribute to the observed differences between these regions. Along the same lines, a second factor is the relatively low basal rate of activity of dentate gyrus granule cells, which could also limit the extent of shared presynaptic–postsynaptic histories at spine pairs (34–36). A third factor is the dendritic response properties and the efficiency of action potential backpropagation (bAP) that differs between dentate granule cells and CA1 pyramidal cells (22, 37, 38).

The combined effect of low basal activity and inefficient bAP may decrease the reliability of shared presynaptic input in shaping synaptic efficacy at dendritic spines of dentate granule cells relative to CA1 pyramidal cells. It may be that the relatively low firing rate also makes Hebbian plasticity processes less effective or relevant in the dentate gyrus than CA1. Lower activity rates in granule cells are believed to shape the response to the deluge of information received from the entorhinal cortex and to aid in pattern separation (36). In fact, a recent computational model of DBS-induced LTP in the MML ascribed the concurrent LTD to the implementation of a global homeostatic rule that could also aid in the pattern separation function of the dentate gyrus. Notably, the results show that spine number and density are unaltered, paralleling the findings presented here, where a shift in the distribution of spine size reflects changes to the existing population (39).

Alternatively, the lower information content per synapse might suggest that the shared activation histories at SDSA pairs are not as relevant to the plasticity processes at play during synaptic plasticity in the dentate gyrus. For example, under normal circumstances, granule cell SDSA synapses may not share as tightly coupled presynaptic and postsynaptic histories as CA1 pairs due to a greater reliance on dendritic computation in

the granule cells over the bAPs that afford precision to plasticity in CA1. It would be interesting to test whether enhancing the bAP with neuromodulators in dentate (40) also increases information content by reducing CV for spines in SDSA pairs. In addition, it would be interesting to follow pairs of spines that grow in response to learning to determine whether they are also contacted by the same axon and then whether subsequent learning serves to enhance their coactivation and growth (41–43). This general hypothesis could be tested by comparing a variety of cell types throughout the brain. The goal would be to determine whether poor backpropagation of APs and low spontaneous activity generally correlate with granular or stellate dendritic arbors and higher CV between paired spines. Contrasts could then be obtained with other cell types that have large apical dendrites, high spontaneous activity, and broad bAPs.

The implications of our findings are twofold. First, they suggest that information storage capacity at synapses varies across brain regions and even within a single structure such as the hippocampus. It will be interesting to learn how this capacity varies across different sections of the dendritic arbor, whether it varies outside the hippocampal formation, and whether that variance correlates with and predicts specific functions. Second, our data reveal that information storage capacity is modifiable by experience, in this case in response to LTP induction. Thus, stimulation and learning paradigms may increase information storage at synapses, and first exposure may prepare synapses for subsequent augmentation of LTP and learning (27–30). Our findings raise the question of whether these rapidly occurring changes persist during the maintenance phase of LTP, which will be investigated in a future study. Determining which of these properties persist and how shifts in the distribution accommodate the underlying computational processes at individual synapses will inform our understanding of basic learning mechanisms in the brain.

Methods

Surgery and Electrophysiology. Data were collected from two young adult male Long–Evans rats aged 121 and 179 d at the time of LTP induction and perfusion. They had been surgically implanted as previously described (23) with wire stimulating electrodes separately into the medial and lateral perforant pathways running in the angular bundle in the LTP hemisphere, and in the medial perforant pathway only in the control hemisphere (only medial path data are described in this paper). Wire field excitatory postsynaptic potential (fEPSP) recording electrodes were implanted bilaterally in the dentate hilus. Two weeks after surgery, baseline recording sessions (30 min) commenced, with animals being in a quiet alert state during the animals' dark cycle. Test pulse stimuli were administered to each pathway as constant-current biphasic square-wave pulses (150-μs half-wave duration) at a rate of 1/30 s, and alternating between the three stimulating electrodes. The test pulse stimulation intensity was set to evoke medial path waveforms with fEPSP slopes >3.5 mV/ms in association with population spike amplitudes between 2 and 4 mV, at a stimulation current ≤500 μA. On the day of LTP induction, after stable baseline recordings were achieved, animals received 30 min of test pulses followed by DBS delivered to the ipsilateral medial perforant path, while the contralateral hippocampus served as a control. The LTP-inducing DBS protocol consisted of five trains of 10 pulses (250-μs half-wave duration) delivered at 400 Hz at a 1-Hz interburst frequency, repeated 10 times at 1-min intervals (23). Test pulse stimulation then resumed until the animal was killed at 30 min after the onset of DBS. The initial slope of the medial path fEPSP (in millivolts per millisecond) was measured for each waveform and expressed as a percentage of the average response during the last 15 min of recording before DBS.

Perfusion and Fixation. At 30 min after the commencement of DBS, animals were perfusion fixed under halothane anesthesia and tracheal supply of oxygen (44). The perfusion involved brief (~20-s) wash with oxygenated Krebs–Ringer Carbicarb buffer [concentration (in mM): 2.0 $CaCl_2$, 11.0 D-glucose, 4.7 KCl, 4.0 $MgSO_4$, 118 NaCl, 12.5 Na_2CO_3, 12.5 $NaHCO_3$; pH 7.4; osmolality, 300–330 mmol/kg], followed by 2% formaldehyde and 2.5% glutaraldehyde (both aldehydes from Ladd Research) in 0.1 M cacodylate buffer (pH 7.4) containing 2 mM $CaCl_2$ and 4 mM $MgSO_4$ for ~1 h (~1,900 mL of fixative was used per animal). The brains were removed from the skull at about 1 h after end of perfusion, wrapped in several layers of cotton gauze, and shipped on ice in the same fixative from the Abraham Laboratory in Dunedin, New Zealand, to the laboratory of K.M.H. in Austin, Texas, by overnight delivery (TNT Holdings B.V.).

Tissue Processing and Serial Sectioning. The fixed tissue was then cut into parasagittal slices (70-μm thickness) with a vibrating blade microtome (Leica Microsystems) and processed for electron microscopy as described previously (44, 45). Briefly, the tissue was treated with reduced osmium (1% osmium tetroxide and 1.5% potassium ferrocyanide in 0.1 M cacodylate buffer) followed by microwave-assisted incubation in 1% osmium tetroxide under vacuum. Then the tissue underwent microwave-assisted dehydration and en bloc staining with 1% uranyl acetate in ascending concentrations of ethanol. The tissue was embedded into LX-112 epoxy resin (Ladd Research) at 60 °C for 48 h before being cut into series of ultrathin sections at the nominal thickness of 45 nm with a 35° diamond knife (DiATOME) on an ultramicrotome (Leica Microsystems). The serial ultrathin sections from MML (region of molecular layer ~125 μm from top of granule cell layer in dorsal blade of the hippocampal dentate gyrus) were collected onto Synaptek Be-Cu slot grids (Electron Microscopy Sciences or Ted Pella), coated with Pioloform (Ted Pella), and stained with a saturated aqueous solution of uranyl acetate followed by lead citrate (46).

Imaging and Alignment. The serial ultrathin sections were imaged, blind as to condition, with either a JEOL JEM-1230 TEM or a transmission-mode scanning EM (tSEM) (Zeiss SUPRA 40 field-emission SEM with a retractable multimode transmitted electron detector and ATLAS package for large-field image acquisition; ref. 44). On the TEM, sections were imaged in two-field mosaics at 5,000× magnification with a Gatan UltraScan 4000 CCD camera (4,080 pixels × 4,080 pixels), controlled by DigitalMicrograph software (Gatan). Mosaics were then stitched with Photomerge function in Adobe Photoshop. The serial TEM images were first manually aligned in Reconstruct (ref. 47; synapseweb.clm.utexas.edu/software-0) and later with Fiji with the TrakEM2 plugin (refs. 48–50; fiji.sc). On the tSEM, each section was imaged with the transmitted electron detector from a single field encompassing 32.768 μm × 32.768 μm (16,384 pixels × 16,384 pixels at 2 nm/pixel resolution). The scan beam was set for a dwell time of 1.3–1.4 ms, with the accelerating voltage of 28 kV in high-current mode. Serial tSEM images were aligned automatically using Fiji with the TrakEM2 plugin. The images were aligned rigidly first, followed by application of affine and then elastic alignment. Images from a series were given a five-letter code to mask the identity of experimental conditions in subsequent analyses with Reconstruct. Pixel size was calibrated for each series using the grating replica image that was acquired along with serial sections. The section thickness was estimated using the cylindrical mitochondria method (51).

Unbiased Reconstructions and Identification of SDSA Pairs. Three dendrites of similar caliber were traced through serial sections from each of the two control and two LTP hemispheres for a total of six dendrites per condition. Dendrite caliber previously has been shown to scale with dendrite cross-section and microtubule count (10, 52). The microtubule count, which is a more reliable measure of caliber, ranged from 30 to 35 and represents the average among all dendrites found in the MML of dentate gyrus (53). These dendritic segments ranged in length from 8.6 to 10.6 μm for the six control dendrites and 9.3 to 10.6 μm for the six LTP dendrites.

Contours were drawn using Reconstruct software on serial images for each spine head. PSDs were identified by their electron density and presence of closely apposed presynaptic vesicles. A total of 209 spines were complete along the control dendrites and 188 spines were complete along the LTP dendrites. These were used for the indicated analyses.

The unbiased dendritic segment analysis involved assessing the number of synapses, SDSAs, and axons interacting with each dendritic segment. Beginning in the center of each of the 12 dendrites, the presynaptic axons were traced past the nearest neighboring axonal bouton until they were determined to form synapses with the same dendrite or a different dendrite. Only the middle portion of the dendrite lengths could be used because only spines in the middle of the dendrite had presynaptic axons sufficiently complete within the series to determine their connectivity. In three cases, one axon made synapses with dendritic spines from two different dendrites in our sample, and these three were included for both dendritic segments.

Each of the 12 dendrites was truncated to contain the central 15–20 spine and shaft synapses with known connectivity. The *z*-trace tool in Reconstruct was used to obtain the unbiased lengths spanning the origin of the first included spine to the origin of the first excluded spine (54). The lengths ranged from 2.8 to 5.9 μm for the six control dendrites and 3.1 to 6.1 μm for the six LTP dendrites. Then the number per micrometer length of dendrite was computed for spines, axons, and SDSAs as illustrated in Fig. 1 *E* and *F*.

PSD areas were measured in Reconstruct according to the orientation in which they were sectioned (18). Perfectly cross-sectioned synapses had distinct presynaptic and postsynaptic membranes, clefts, and docked vesicles, and their areas were calculated by summing the product of PSD length and section thickness for each section spanned. En face synapses were cut parallel to the PSD surface, appeared in one section, and were measured as the enclosed area on that section. Obliquely sectioned PSDs were measured as the sum of the total cross-sectioned areas and total en face areas without overlap on adjacent sections. Then the synapse areas were summed along the truncated, unbiased dendritic length to compute values illustrated in Fig. 3.

Segmentation and Evaluation of Spines. Blender, a free, open-source, user-extensible computer graphics tool, was used in conjunction with 3D models generated in Reconstruct. We enhanced our Python add-on to Blender, Neuropil Tools (18), with a new Processor Tool to facilitate the processing of the 3D reconstruction and evaluation of spines. The additions encompassed in Processor Tool were as follows:

i) The software allows for the selection of traced objects from Reconstruct (.ser) files by filter, allowing the user to select only desired contour traces (in this case spine head and PSD contours for three dendrites per series).
ii) At the press of a button, the tool generates 3D representations of selected contours in Blender. This step invokes functions from VolRoverN (55) from within Blender, to generate mesh objects by the addition of triangle faces between contour traces.
iii) Smoothing and evening of the surface of spine objects is accomplished with GAMer (fetk.org/codes/gamer/) software.
iv) In a few cases, the formation of triangles was uneven and required additional manipulation by Blender tools and repeating of step *iii* before proceeding to step *v*.
v) Last, PSD areas are assigned as metadata (represented by red triangles) on reconstructed spine heads; the assignment is performed based on the overlap of PSD and spine head contours (described above) in 3D space.

Dendritic spines were segmented as previously described (18) using the Neuropil Tools analyzer tool. We focused on spine volumes because they had proven to be the most consistently measured dimension among the correlated metrics of spine head volume, synaptic area, and vesicle number (18). The edges of the synaptic contact areas are less precisely determined in oblique sections, and vesicles can be buried within the depth of a section or span two sections and, hence, are less reliably scored. The selection of spine head from spine neck and from spine neck to dendritic shaft were made using the same standardized criterion as before (visually identified as halfway along the concave arc as the head narrows to form the neck). Spines were excluded if they were clipped by the edge of the image dataset. To ensure the accuracy of the measurements, segmentation and spine head volume evaluation were completed four times (twice each by two people) and averaged. A further check was added at this step, whereby spine heads with a CV $\geq$ 0.02 for all four measurements were visually evaluated by an expert, and any discrepancy in the segmentation was corrected. Interestingly, the only spines with a CV larger than 0.02 were in the LTP condition. We believe this occurs because the spines undergoing LTP are likely to be in transition at the 30-min time point, and as such the delineation between spine head and spine neck is more difficult for the human eye to see. In the two control condition series, further evaluation by an expert was performed, and adjustments were made accordingly (Fig. 2 and Fig. S4).

Statistical Analysis. Statistical analysis and plots were generated using Python 3.4 with NumPy, SciPy, and Matplotlib. Cumulative distributions (CDFs) were generated and plotted using spine head volume measurements output from Neuropil Tools. Due to the skewed (nonnormal) distribution of the data, the KS test, a nonparametric test, was used for comparing distributions. The CV for SDSA pairs was calculated from the SD of the spine pair divided by the mean volume of the spine pair. The CV was calculated for each of the SDSA spine pairs ($n = 2$) and because the entire population was thus utilized, we made our CV calculations using N rather than N–1, the latter being most appropriate when sampling from a population. The median CV for each series or condition was the median of the CV of included SDSA pairs. ANCOVAs were used to test for differences in the slopes between SDSA pairs and random pairs of spines. Two sets of 125 random pairs of spine head volumes were created from the population of MML control and LTP spines. The random pairs of spines were generated by sampling randomly with replacement from each respective population, using Python to generate random combinations of two spines at a time.

Estimation of Number of Distinguishable Spine Sizes and Bits of Precision in Spine Size. To estimate the number of distinguishable spine sizes and bits of precision, we calculated the number of distinct Gaussian distributions of spine sizes, each with a certain mean size and SD that together would cover and span the entire range of spine head sizes for each series or condition. Given the CV in head size between coactivated (SDSA) synapses, the spacing between the mean values of each subdistribution can be chosen to achieve a total of 31% overlap with adjacent subdistributions having a 69% discrimination threshold. A 69% discrimination threshold is commonly used in the field of psychophysics and corresponds to a signal-to-noise ratio of 1 (31). The 69% confidence interval, z, of a Gaussian distribution is given (using the inverse error function, erf^{-1}) by the following:

$$z = \mathrm{sqrt}(2) * \mathrm{erf}^{-1}(0.69).$$

The spacing, s, of adjacent intervals of mean, μ, is given by the following:

$$s = \mu * 2 * \mathrm{CV} * z.$$

The number, N, of such distributions that would span the range (R = largest/smallest spine head) for a range of spine sizes is as follows:

$$N = \log(R)/\log(1 + 2 * \mathrm{CV} * z),$$

where the median CV = 0.46 (control) and 0.26 (LTP) and R = 73.3 (control) and 236.2 (LTP) and gives the following outcomes:

$$N = 6.5(\mathrm{control}), \quad N = 12.9(\mathrm{LTP}).$$

The number of bits of precision implied by N distinguishable distributions is given by the following:

$$\mathrm{bits} = \log_2(N),$$
$$\mathrm{bits} = 2.7(\mathrm{control}), \quad \mathrm{bits} = 3.7(\mathrm{LTP}).$$

ACKNOWLEDGMENTS. Sara Mason-Parker is thanked for technical assistance in electrophysiology and perfusions. Bob Smith and Libby Perry are thanked for initial serial sectioning and TEM imaging. We thank Amy Pohodich and Ryan Ellis for their participation in some of the early reconstructions, later curated by P.H.P. This study was supported by NIH Grants NS21184, MH095980, and MH104319, and National Science Foundation NeuroNex Grant 1707356 (to K.M.H.); Grants GM103712 and MH079076 (to T.J.S.); a University of Otago postgraduate scholarship (to J.B.B.); the Texas Emerging Technologies Fund; and the Howard Hughes Medical Institute.

1. Bi GQ, Poo MM (1998) Synaptic modifications in cultured hippocampal neurons: Dependence on spike timing, synaptic strength, and postsynaptic cell type. *J Neurosci* 18: 10464–10472.
2. Caporale N, Dan Y (2008) Spike timing-dependent plasticity: A Hebbian learning rule. *Annu Rev Neurosci* 31:25–46.
3. Lisman J (2017) Glutamatergic synapses are structurally and biochemically complex because of multiple plasticity processes: Long-term potentiation, long-term depression, short-term potentiation and scaling. *Philos Trans R Soc Lond B Biol Sci* 372: 1715.
4. Harris KM, Stevens JK (1989) Dendritic spines of CA 1 pyramidal cells in the rat hippocampus: Serial electron microscopy with reference to their biophysical characteristics. *J Neurosci* 9:2982–2997.
5. Lisman JE, Harris KM (1993) Quantal analysis and synaptic anatomy—integrating two views of hippocampal plasticity. *Trends Neurosci* 16:141–147.
6. Schikorski T, Stevens CF (1997) Quantitative ultrastructural analysis of hippocampal excitatory synapses. *J Neurosci* 17:5858–5867.
7. Murthy VN, Schikorski T, Stevens CF, Zhu Y (2001) Inactivity produces increases in neurotransmitter release and synapse size. *Neuron* 32:673–682.
8. Branco T, Staras K, Darcy KJ, Goda Y (2008) Local dendritic activity sets release probability at hippocampal synapses. *Neuron* 59:475–485.
9. Nikonenko I, et al. (2008) PSD-95 promotes synaptogenesis and multiinnervated spine formation through nitric oxide signaling. *J Cell Biol* 183:1115–1127.
10. Bourne JN, Harris KM (2011) Coordination of size and number of excitatory and inhibitory synapses results in a balanced structural plasticity along mature hippocampal CA1 dendrites during LTP. *Hippocampus* 21:354–373.
11. Bourne JN, Chirillo MA, Harris KM (2013) Presynaptic ultrastructural plasticity along CA3→CA1 axons during long-term potentiation in mature hippocampus. *J Comp Neurol* 521:3898–3912.
12. Meyer D, Bonhoeffer T, Scheuss V (2014) Balance and stability of synaptic structures during synaptic plasticity. *Neuron* 82:430–443.
13. Smith HL, et al. (2016) Mitochondrial support of persistent presynaptic vesicle mobilization with age-dependent synaptic growth after LTP. *eLife* 5:e15275.

14. Chicurel ME, Harris KM (1992) Three-dimensional analysis of the structure and composition of CA3 branched dendritic spines and their synaptic relationships with mossy fiber boutons in the rat hippocampus. *J Comp Neurol* 325:169–182.
15. Kasthuri N, et al. (2015) Saturated reconstruction of a volume of neocortex. *Cell* 162: 648–661.
16. Markram H, Lübke J, Frotscher M, Roth A, Sakmann B (1997) Physiology and anatomy of synaptic connections between thick tufted pyramidal neurones in the developing rat neocortex. *J Physiol* 500:409–440.
17. Sorra KE, Harris KM (1993) Occurrence and three-dimensional structure of multiple synapses between individual radiatum axons and their target pyramidal cells in hippocampal area CA1. *J Neurosci* 13:3736–3748.
18. Bartol TM, et al. (2015) Nanoconnectomic upper bound on the variability of synaptic plasticity. *eLife* 4:e10778.
19. Saxe MD, et al. (2006) Ablation of hippocampal neurogenesis impairs contextual fear conditioning and synaptic plasticity in the dentate gyrus. *Proc Natl Acad Sci USA* 103: 17501–17506.
20. Snyder JS, Kee N, Wojtowicz JM (2001) Effects of adult neurogenesis on synaptic plasticity in the rat dentate gyrus. *J Neurophysiol* 85:2423–2431.
21. Lopez-Rojas J, Heine M, Kreutz MR (2016) Plasticity of intrinsic excitability in mature granule cells of the dentate gyrus. *Sci Rep* 6:21615.
22. Krueppel R, Remy S, Beck H (2011) Dendritic integration in hippocampal dentate granule cells. *Neuron* 71:512–528.
23. Bowden JB, Abraham WC, Harris KM (2012) Differential effects of strain, circadian cycle, and stimulation pattern on LTP and concurrent LTD in the dentate gyrus of freely moving rats. *Hippocampus* 22:1363–1370.
24. Engert F, Bonhoeffer T (1999) Dendritic spine changes associated with hippocampal long-term synaptic plasticity. *Nature* 399:66–70.
25. Abraham WC, Logan B, Wolff A, Benuskova L (2007) "Heterosynaptic" LTD in the dentate gyrus of anesthetized rat requires homosynaptic activity. *J Neurophysiol* 98: 1048–1051.
26. White G, Levy WB, Steward O (1990) Spatial overlap between populations of synapses determines the extent of their associative interaction during the induction of long-term potentiation and depression. *J Neurophysiol* 64:1186–1198.
27. Cao G, Harris KM (2014) Augmenting saturated LTP by broadly spaced episodes of theta-burst stimulation in hippocampal area CA1 of adult rats and mice. *J Neurophysiol* 112: 1916–1924.
28. Kramár EA, et al. (2012) Synaptic evidence for the efficacy of spaced learning. *Proc Natl Acad Sci USA* 109:5121–5126.
29. Babayan AH, et al. (2012) Integrin dynamics produce a delayed stage of long-term potentiation and memory consolidation. *J Neurosci* 32:12854–12861.
30. Bell ME, et al. (2014) Dynamics of nascent and active zone ultrastructure as synapses enlarge during long-term potentiation in mature hippocampus. *J Comp Neurol* 522: 3861–3884.
31. Schmidt-Hieber C, Jonas P, Bischofberger J (2007) Subthreshold dendritic signal processing and coincidence detection in dentate gyrus granule cells. *J Neurosci* 27: 8430–8441.
32. Buzsáki G, Mizuseki K (2014) The log-dynamic brain: How skewed distributions affect network operations. *Nat Rev Neurosci* 15:264–278.
33. Mongiat LA, Schinder AF (2011) Adult neurogenesis and the plasticity of the dentate gyrus network. *Eur J Neurosci* 33:1055–1061.
34. Chawla MK, et al. (2005) Sparse, environmentally selective expression of Arc RNA in the upper blade of the rodent fascia dentata by brief spatial experience. *Hippocampus* 15: 579–586.
35. Mizuseki K, Diba K, Pastalkova E, Buzsáki G (2011) Hippocampal CA1 pyramidal cells form functionally distinct sublayers. *Nat Neurosci* 14:1174–1181.
36. Neunuebel JP, Knierim JJ (2012) Spatial firing correlates of physiologically distinct cell types of the rat dentate gyrus. *J Neurosci* 32:3848–3858.
37. Brunner J, Szabadics J (2016) Analogue modulation of back-propagating action potentials enables dendritic hybrid signalling. *Nat Commun* 7:13033.
38. Green DM, Swets JA (1966) *Signal Detection Theory and Psychophysics* (Peninsula Publishing, Los Altos, CA).
39. Jedlicka P, Benuskova L, Abraham WC (2015) A voltage-based STDP rule combined with fast BCM-like metaplasticity accounts for LTP and concurrent "heterosynaptic" LTD in the dentate gyrus in vivo. *PLoS Comput Biol* 11:e1004588.
40. Yang K, Dani JA (2014) Dopamine D1 and D5 receptors modulate spike timing-dependent plasticity at medial perforant path to dentate granule cell synapses. *J Neurosci* 34:15888–15897.
41. Xu T, et al. (2009) Rapid formation and selective stabilization of synapses for enduring motor memories. *Nature* 462:915–919.
42. Landers MS, Knott GW, Lipp HP, Poletaeva I, Welker E (2011) Synapse formation in adult barrel cortex following naturalistic environmental enrichment. *Neuroscience* 199:143–152.
43. Kastellakis G, Cai DJ, Mednick SC, Silva AJ, Poirazi P (2015) Synaptic clustering within dendrites: An emerging theory of memory formation. *Prog Neurobiol* 126:19–35.
44. Kuwajima M, Mendenhall JM, Harris KM (2013) Large-volume reconstruction of brain tissue from high-resolution serial section images acquired by SEM-based scanning transmission electron microscopy. *Methods Mol Biol* 950:253–273.
45. Harris KM, et al. (2006) Uniform serial sectioning for transmission electron microscopy. *J Neurosci* 26:12101–12103.
46. Reynolds ES (1963) The use of lead citrate at high pH as an electron-opaque stain in electron microscopy. *J Cell Biol* 17:208–212.
47. Fiala JC (2005) Reconstruct: A free editor for serial section microscopy. *J Microsc* 218: 52–61.
48. Cardona A, et al. (2012) TrakEM2 software for neural circuit reconstruction. *PLoS One* 7:e38011.
49. Saalfeld S, Fetter R, Cardona A, Tomancak P (2012) Elastic volume reconstruction from series of ultra-thin microscopy sections. *Nat Methods* 9:717–720.
50. Schindelin J, et al. (2012) Fiji: An open-source platform for biological-image analysis. *Nat Methods* 9:676–682.
51. Fiala JC, Harris KM (2001) Cylindrical diameters method for calibrating section thickness in serial electron microscopy. *J Microsc* 202:468–472.
52. Fiala JC, et al. (2003) Timing of neuronal and glial ultrastructure disruption during brain slice preparation and recovery in vitro. *J Comp Neurol* 465:90–103.
53. Bowden JB, Mendenhall JM, Abraham WC, Harris KM (2008) Microtubule number as a correlate of dendritic spine density in dentate granule cells. *Soc Neurosci Abstr* 34: 636.20.
54. Fiala JC, Harris KM (2001) Extending unbiased stereology of brain ultrastructure to three-dimensional volumes. *J Am Med Inform Assoc* 8:1–16.
55. Edwards J, et al. (2014) VolRoverN: Enhancing surface and volumetric reconstruction for realistic dynamical simulation of cellular and subcellular function. *Neuroinformatics* 12: 277–289.